Northumbria Research Link

Citation: Shao, Zengkai, Zhu, Jiangbo, Zhang, Yanfeng, Chen, Yujie and Yu, Siyuan (2018) On-chip switchable radially and azimuthally polarized vortex beam generation. Optics Letters, 43 (6). p. 1263. ISSN 0146-9592

Published by: OSA

URL: https://doi.org/10.1364/OL.43.001263 <https://doi.org/10.1364/OL.43.001263>

This version was downloaded from Northumbria Research Link: http://nrl.northumbria.ac.uk/id/eprint/43291/

Northumbria University has developed Northumbria Research Link (NRL) to enable users to access the University's research output. Copyright © and moral rights for items on NRL are retained by the individual author(s) and/or other copyright owners. Single copies of full items can be reproduced, displayed or performed, and given to third parties in any format or medium for personal research or study, educational, or not-for-profit purposes without prior permission or charge, provided the authors, title and full bibliographic details are given, as well as a hyperlink and/or URL to the original metadata page. The content must not be changed in any way. Full items must not be sold commercially in any format or medium without formal permission of the copyright holder. The full policy is available online: http://nrl.northumbria.ac.uk/policies.html

This document may differ from the final, published version of the research and has been made available online in accordance with publisher policies. To read and/or cite from the published version of the research, please visit the publisher's website (a subscription may be required.)

Northumbria University NEWCASTLE

CUSTOMER SERVICE EXCELLENCE CSE

UniversityLibrary

On-chip switchable radially and azimuthally polarized vortex beam generation

Zengkai Shao,[1] Jiangbo Zhu,[2] Yanfeng Zhang,[1,*] Yujie Chen,[1] and Siyuan Yu[2,*]

[1]State Key Laboratory of Optoelectronic Materials and Technologies, School of Electronics and Information Technology, Sun Yat-sen University, Guangzhou 510275, China
[2]Photonics Group, Merchant Venturers School of Engineering, University of Bristol, Bristol BS8 1UB, UK
**Corresponding authors: zhangyf33@mail.sysu.edu.cn; s.yu@bristol.ac.uk*

Cylindrical vector vortex (CVV) beams, complex light fields that exhibit a vector nature and carry quantized orbital angular momentum (OAM) states, have been widely investigated due to their rich applications. Current technologies to generate CVV beams using individual polarization and spatial phase manipulations suffer from bulky size and low configurability. In this work, we propose and experimentally demonstrate an approach to generate CVV beams with a single integrated device based on silicon nitride microring resonator and embedded top-gratings. The device allows the manipulation on both the polarization and OAM degrees of freedom of light and enables the generation of both radially and azimuthally polarized CVV beams. In addition, we develop a method to fabricate the devices of shallow-etched top-gratings with only one-step etching. This novel method provides new capabilities to develop on-chip integrated devices with great ease and flexibility.

Cylindrical vector beams are vector solutions of Maxwell's equations with an inhomogeneous but cylindrically symmetric polarization distribution in the transverse plane. Meanwhile, optical vortex beams with spiral wave fronts have also attracted much interest as they carry intrinsic orbital angular momentum (OAM) of light [1-3]. Cylindrical vector vortex (CVV) beams combining the characteristics of spatial polarization variation and helical phase fronts provide the extra degree of freedom for light manipulation that has been widely used as new promising resources in many applications [4-7]. Radially polarized (RP) and azimuthally polarized (AP) vortex beams are distinctive CVV beams due to their unique focusing properties and focal components enabling a variety of new features such as sharper focusing [8], and Gouy phase shift [9]. Several approaches depending on bulk optical elements [10] and compact optical metamaterials [11,12] have been proposed to generate CVV beams. However, these systems could not be straightforwardly applied in photonic integrated circuit (PIC).

Recently, on-chip integrated emitters are proposed and demonstrated to generate vector vortex beams [13]. Despite achievement of reliability and tunability in the emitted topological charge, less attention is paid to the control of both spatial phase and polarization. For example, silicon microring-based emitters with gratings embedded along the inner-sidewall (or on top) of the ring resonator, typically generate vortex beams with fixed azimuthal (or radial) polarization [13-15]. In a recent work, we have demonstrated the interaction between transverse spin angular momentum in evanescent waves and the intrinsic OAM in vortex beams by tailoring a silicon nitride (SiN_x) micro-ring waveguide [16]. Vortex beams with a large range of polarization states are generated by engineering the transverse spin in evanescent waves, while it is still challenging to reconfigure the emitted polarization state on individual devices. Generating adjustable radially and azimuthally polarized vortex beams on a single device is still challenging. However, CVV beams emitters of high configurability in both topological charge and polarization state are highly desirable for many practical applications.

In this work, we propose an approach to generate CVV beams using a SiN_x micro-ring resonator with shallow-etched periodic angular gratings placed on top of the ring waveguide. This device can be configured to generate both radially and azimuthally polarized vector beams of broadband well-defined OAM states by simply switching the polarization and wavelength of the inject light, which is experimentally demonstrated as designed. In addition, the angular top-gratings are shallow-etched in a one-step process, which simplifies the complexity of fabrication process. The proposed approach provides an extremely simple and flexible on-chip solution to generate switchable radially and azimuthally polarized vortex beams.

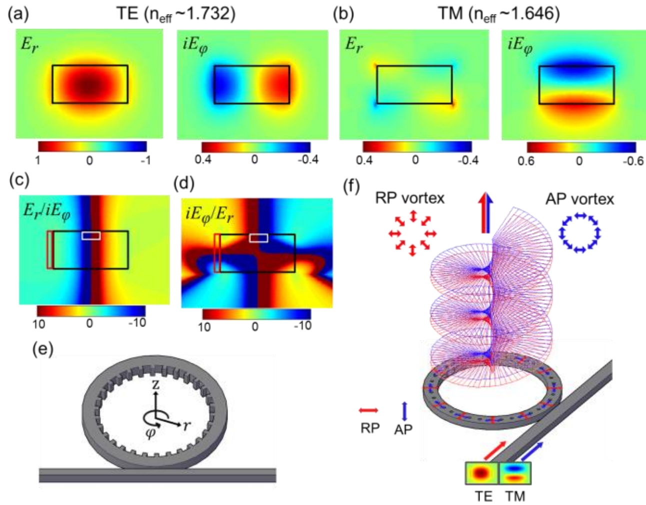

Fig. 1. Simulated cross-sectional field distributions of the radial component E_r and azimuthal component iE_φ for (a) TE mode and (b) TM mode in a SiN_x waveguide at 1550 nm. The corresponding distribution of the component ratio (c) E_r/iE_φ for TE mode and (d) iE_φ/E_r for TM mode. Schematic of the designed vortex beam device in our previous work (e) and in this work (f).

WGMs in a ring cavity carry high-order OAM states [17]. By introducing angular gratings or download waveguides array [18], the confined WGMs in the ring cavity can be coupled into radiative cylindrical modes. In addition, the state of polarization (SoP) of the radiated CVV beams is determined by the SoP of the local optical field being scattered at each grating element [13]. Using a finite difference eigenmode (FDE) solver, we simulated the cross-sectional electric field distribution of fundamental TE mode and TM mode in a SiN_x waveguide, as shown in Figs. 1(a) and 1(b). The designed SiN_x micro-ring waveguide has a cross-section of 1.2 μm in width and 580 nm in height in order to achieve strong confinement for both TE and TM modes. The waveguide is fabricated on a 5-μm-thick thermal-oxide silicon substrate and surrounded by air. Silicon nitride has a moderate refractive index of ~2.0, affording high fabrication tolerance and low phase sensitivity. The calculated effective refractive indices are n_{eff} = 1.723 for fundamental TE mode and n_{eff} = 1.646 for fundamental TM mode at λ = 1550 nm. For the TE mode, apart from E_r, a strong azimuthal component E_φ at the lateral core-cladding interface (sidewalls) can also be observed in ±π/2 phase difference to E_r, while E_φ is negligible at the centre of the waveguide. For TM mode, strong E_φ exists at the upper and lower core-cladding interfaces, while E_r is negligible at the center of the waveguide. Figs. 1(c) and 1(d) show the calculated E_r/iE_φ for TE mode and iE_φ/E_r for TM mode, respectively. In our previous work [18], the angular grating elements are located at the inner sidewall of the waveguide, shown in Fig. 1(e), where the amplitude of E_r and iE_φ are comparable (E_r/iE_φ ~ 1.25) for TE mode [marked in Fig. 1(c) by the red box]. It is very difficult to eliminate one of electric components by tailoring waveguide dimensions to generate pure RP or AP vortex beams.

With the local field of the TE and TM modes at the upper core-cladding boundary of the waveguide dominated by E_r and E_φ, respectively, placing the gratings at the top [e.g., within the region marked by the white box in Figs. 1(c) and 1(d)] allows for the generation of AP and RP vortex beams by simply switching the mode (i.e., TE or TM) in the ring. In addition, the topological charge of radiated vortex beam l satisfies the selection rule of $l = p - q$ (where p is the WGMs order in the ring, q is the number of grating elements around the resonator), which can be tuned by simply changing the input wavelength so that it aligns with different ring cavity resonances. Shallow-etched holes are used as periodic angular gratings on the top of the waveguide, shown in Fig. 1(f). With these gratings arranged in a second-order grating fashion, the first-order diffracted light from the WGMs collectively produce a vortex beam carrying optical OAM and propagating perpendicular to the resonator plane, with a SoP of RP or AP depending on the mode in the ring waveguide being TE or TM mode.

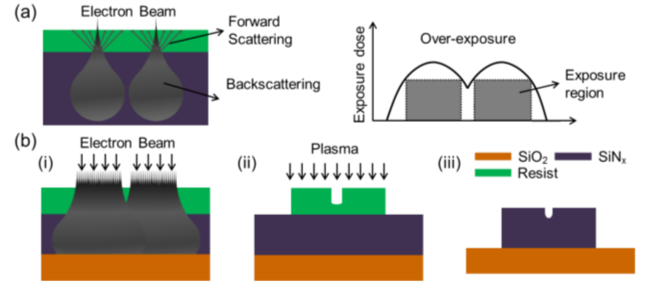

Fig. 2. (a) Left: Schematic of the electrons distribution during the E-beam lithography resulting from forward scattering and backscattering predominantly. Right: Curve of the exposure dose with over-exposure of the gap between waveguides. (b) Fabrication process of the proposed structure. (i) Exposure of the patterns by EBL. (ii) RIE process after development of resist. (iii) Lift-off the resist.

In general, the proposed device with shallow-holes as a three-dimensional microstructure can be fabricated by many technologies, such as gray-scale lithography [19], photoresist reflow processing [20], and multi-step etching [21]. However, those methods increase the complexity of the fabrication process and have special requirements for the photoresist. Here, we develop a simple method to etch through the 580-nm thick SiN_x waveguide with the embedded shallow-holes in a one-step process utilizing a combination of the over-exposure of negative resist resulting from forward scattering and backscattering of electrons during the E-beam lithography (EBL) [shown in Fig. 2(a)] [22] and the lag-effect [23] during the reactive-ion etching (RIE) process. Figure 2(b) shows details of the fabrication process. In our experiment, the 580-nm SiN_x layer is deposited on a thermally oxidized <100> silicon wafer with an oxide thickness of 5 μm using an inductively-coupled plasma chemical vapour deposition (ICP-CVD) process [24]. A 480-nm-thick negative resist (diluted AZ nLOF 2035 from Clariant Corporation) is used to pattern structures with the EBL system at 100 kV.

To achieve appropriate shallow-etched holes, a series of slot waveguides with different gap widths (from 80 nm to 300 nm in 20-nm steps) are examined under an optimized exposure dose of 170 $\mu c/cm^2$. The over-all view and zoom-in cross-section of photoresist profiles after development are shown in Figs. 3(a) and 3(b), respectively. It can be seen that under such conditions, gaps of 180 nm and above can be fully developed and etched through by the subsequent RIE process, shown in Fig. 3(c). Patterns of 120 nm- and 140 nm-gap can be distinguished with obvious residual photoresist even after RIE etching, therefore leaving the SiN_x unetched. When the gap is 160 nm, appropriate over-exposure is achieved resulting in a shallow-etched pattern into the SiN_x after RIE [marked by a red

box in Figs. 3(b) and (c)]. A smooth and narrower profile at the bottom of the etched slot is observed due to the lag-effect during the RIE process, which helps to reduce the perturbation on the field distribution in the waveguide and reduce the propagation loss of both TE and TM modes. Figure 3(d) shows the zoom-in view of a CVV beams emitter fabricated by this method. The SiN_x ring resonator has a radius of 60 μm. The gap between the access waveguide and the ring is fixed as 210 nm. The number of periodic shallow-holes is fixed at q = 420 with the calculated zero topology charge (l = 0) at λ = 1550 nm for TE mode and λ = 1495 nm for TM mode.

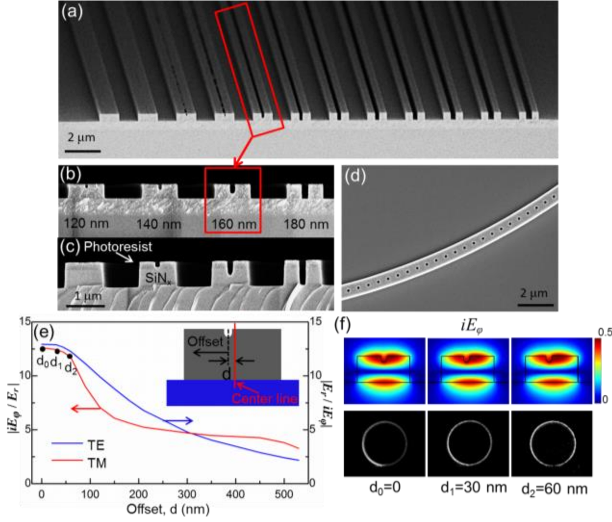

Fig. 3. (a) SEM image of the photoresist patterns after the E-beam lithography and development. Zoom-in cross-section of patterns (b) before and (c) after etching through a 580-nm SiN_x layer by the RIE process. (d) Zoom-in view of the fabricated device. (e) Calculated curves of $|E_r/iE_\varphi|$ and $|iE_\varphi/E_r|$ for TE and TM mode versus the offset of the shallow-etched holes on the top of the waveguide. Inset: schematic of the local offset. (f) Calculated field distributions of the azimuthal component iE_φ and measured near-field intensity for TM mode when d=0, 30 nm, 60 nm, respectively.

Note that the coupling strength between gratings and microring is highly sensitive to the size and relative location of the gratings [15, 25]. The diameter of the shallow-etched holes here is fixed at 160 nm as mentioned above. Similarly, to achieve a decent near-field intensity profile of the generated vortex beam as well as high purity of polarization, devices with holes of various offsets (d) to the center of waveguide are considered, as shown in Figs. 3(e) and 3(f). The calculated curve of $|E_r/iE_\varphi|$ ($|iE_\varphi/E_r|$) for TE (TM) mode is rapidly decreasing as $d > 60$ nm in Fig. 3(e), especially for TM mode, indicating low purity of radial (azimuthal) polarization. While placing holes of this size at the top center the angular gratings results in high scattering coefficient as seen in the quick decay of intensity along the cavity, which greatly disrupts the cavity resonance [as shown in Fig. 3(f) with d_0 = 0]. Such intensity inhomogeneity would degrade the mode purity. Therefore, a slight offset of d_2 = 60 nm is chosen to achieve relative uniform angular intensity distribution as well as high purity of polarization, which is employed for devices in the following experiments.

The experimental characterizations of the device are performed with the setup shown in Fig. 4(a). A coupler with the energy ratio of 99:1 is used to divide the input beam into two beams. The one with larger power is connected to the lensed fiber and then coupled to the integrated device, while the smaller one is tuned into a right-hand circularly polarized (RHCP) or left-hand circularly polarized (LHCP) reference beam with a collimator, a 1/4 waveplate, and a polarizer. A variable optical attenuator (VOA) is used to balance the powers of the two interfering paths additionally. The vertically emitted beam from the device plane is collected and collimated with a 20X objective lens positioned in the working distance (1.7 mm) away from the device. The emission spectral response of the emitter is obtained by scanning the wavelength of the input laser (1530-1580 nm), shown in Fig. 4(b). Here, considering a 5.4-dB insert loss for objective lens, with the measured data being normalized to the input power, the emission efficiency of each OAM state can be estimated from the power spectrum directly [13]. For example, for l = -3 at λ = 1562.2 nm (TE mode), the output power is around -10.5 dBm, then the efficiency at l = -3 can be obtained as η = -10.5 dB or 8.93%. The measured emission efficiency across the experimental wavelength range is 5.5% ~ 10.1% for TE mode and 5.2% ~ 11.9% for TM mode. Note that emission power is decreased at the resonance wavelength near l = 0 for TE mode, which is the result of strong scattering and coupling between adjacent modes. The mode splitting near 1553.4 nm for TE mode and near 1510.4 nm (not shown in the figure) for TM mode is observed, which is the signature of l = 0, due to the Bragg back-reflection of the grating. These wavelengths are consistent with the simulation results, demonstrating the high fabrication tolerance of SiN_x devices.

The first column of Fig. 4(c) shows the near-field intensity profiles of the generated vortex beam for TE mode and TM mode, respectively. Then an analyzing polarizer is used to examine the polarization states of the vortex beams. The measured intensity distributions after passing through the analyzing polarizer in horizontal, 45°, vertical, and −45° orientations are shown in Fig. 4(c). The intensity distributions of the two symmetric lobes for TE (TM) mode are parallel (perpendicular) to the trans-axis of the polarizer, confirming that the vortex beam is in radial (azimuthal) polarization.

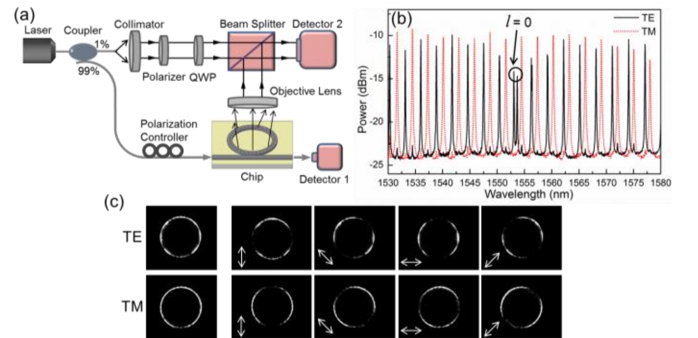

Fig. 4. (a) Experimental setup for device characterization. (b) Measured power (normalized) by scanning the input light wavelength with switching the polarization of excited WGMs. (c) Measured near-field intensity patterns after passing through a polarizer with different polarization angles for TE mode and TM mode, respectively. The polarization angles are denoted by double-headed arrows in white.

To further accurately confirm the polarized component of the vortex beams, a radial polarization converter (RPC) is utilized to selectively measure the power of RP and AP components [26].

Figure 5(a) shows the schematic of the experimental method consisting of a RPC and a linear polarizer (LP). The RPC can be typically used for its spatially varying anisotropy to convert linearly polarized light into vector beams of azimuthal or radial polarizations. Here the reversed effect of this element is employed: by injecting the light into the exit side, RP and AP components in the vortex beam will be converted into horizontally- and vertically-polarized light leaving the entrance side, respectively. Followed by a rotatable polarizer, the RP and AP components are filtered in 0° and 90° orientations, and then imaged by an infra-red camera, respectively, shown in Fig. 5(b). It is evident that the emitted beam by launching TE (TM) mode is predominantly transformed into horizontally- (vertically-) polarized beam, indicating the generation of the radially (azimuthally) polarized vortex beams.

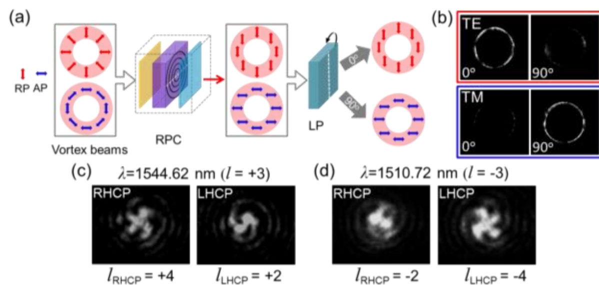

Fig. 5. (a) Schematic of the measurement method. (b) Near-field intensity distributions of the vortex beam through the RPC element and linear polarizer for TE and TM modes, respectively. (c) (d) Measured interference patterns with RHCP and LHCP reference beams.

In addition, the signature spiral wavefront and the topological charge of optical vortex are verified. It has been analyzed that the AP and RP vortex beams can be described as the superposition of two orthogonal scalar vortices which consist of a RHCP beam with topological charge of ($l + 1$) and a LHCP beam with ($l - 1$) [27]. The value and sign of l would be observed by interfering the generated beam with a co-propagating LHCP or RHCP Gaussian beam as reference [12]. For TE mode at λ = 1544.62 nm (l = +3) and TM mode at λ = 1510.72 nm (l = -3), the measured interference patterns with RHCP and LHCP reference beams are shown in Figs. 5(c) and 5(d), respectively. The number of spiral arms agrees well with the prediction for both TE and TM modes.

In summary, we have demonstrated an integrated device that emits cylindrical vector vortex beams based on a SiN_x micro-ring with shallow-etched angular gratings on top of the ring waveguide. The device exploits the large difference of the radial and azimuthal electric distributions between excited TE mode and TM mode in the waveguide. It is capable of being configured to generate both radially and azimuthally polarized vector beams as well as broadband OAM states by simply switching the polarization and wavelength of the input light. Our approach provides a simple and feasible solution for an integrated cylindrical vortex beam switch and may open a new path for practical applications of the structured beams in emerging areas including nanoparticle trapping, optical communications, and quantum optics.

Funding. SYSU is supported by National Natural Science Foundations of China (61490715, U1701661, 11774437, 61323001，11690031), National Basic Research Program of China (973 Program) (2014CB340000), National Key Research and Development Program of China (2016YFB0402503), and Science and Technology Program of Guangzhou (201707020017). UoB is supported by European Union Horizon2020 project ROAM.

References

1. A. M. Yao and M. J. Padgett, Adv. Opt. Photon. **3**, 161 (2011).
2. L. Allen, M. W. Beijersbergen, R. J. C. Spreeuw, and J. P. Woerdman, Phys. Rev. A **45**, 8185 (1992).
3. Q. Zhan, Adv. Opt. Photonics **1**, 1 (2009).
4. Z. Zhao, J. Wang, S. Li, and A. E. Willner, Opt. Lett. **38**, 932 (2013).
5. V. D'Ambrosio, G. Carvacho, F. Graffitti, C. Vitelli, B. Piccirillo, L. Marrucci, and F. Sciarrino, Phys. Rev. A **94**, 030304 (2016).
6. V. Parigi, V. D'Ambrosio, C. Arnold, L. Marrucci, F. Sciarrino, and J. Laurat, Nat. Commun. **6**, 7706 (2015).
7. J. Wang, J. Y. Yang, I. M. Fazal, N. Ahmed, Y. Yan, H. Huang, Y. Y. Ren, Y. Yue, S. Dolinar, M. Tur, and A. E. Willner, Nat. Photonics **6**, 488 (2012).
8. L. Rao, J. Pu, Z. Chen, and P. Yei, Opt. Laser Technol. **41**, 241 (2009).
9. Y. Zhang, X. Guo, L. Han, P. Li, S. Liu, H. Cheng, and J. Zhao, Opt. Express **25**, 25725 (2017).
10. Y. S. Rumala, G. Milione, T. A. Nguyen, S. Pratavieira, Z. Hossain, D. Nolan, S. Slussarenko, E. Karimi, L. Marrucci, R. R. Alfano, Opt. Lett. **38**, 5083 (2013).
11. F. Yue, D. Wen, J. Xin, B. D. Gerardot, J. Li, and X. Chen, ACS photonics **3**, 1558 (2016).
12. M. Kang, J. Chen, X. Wang, and H. Wang, J. Opt. Soc. Am. B **29**, 572 (2012).
13. X. Cai, J. Wang, M. J. Strain, B. J. Morris, J. Zhu, M. Sorel, J. L. O'Brien, M. G. Thompson, and S. Yu, Science **338**, 363 (2012).
14. M. J. Strain, X. Cai, J. Wang, J. Zhu, D. B. Phillips, L. Chen, M. Lopez-Garcia, J. L. O'Brien, M. G. Thompson, M. Sorel, and S. Yu, Nat. Commun. **5**, 4856 (2014).
15. R. Li, X. Feng, D. Zhang, K. Cui, F. Liu, and Y. Huang, IEEE Photonics J. **6**, 1 (2014).
16. Z. Shao, J. Zhu, Y. Chen, Y. Zhang, and S. Yu, arXiv: 1709.09811 [physics.optics] (2017).
17. A. B. Matsko, A. A. Savchenkov, D. Strekalov, and L. Maleki, Phys. Rev. Lett. **95**, 143904 (2005).
18. D. Zhang, X. Feng, and Y. Huang, Opt. Express **20**, 26986 (2012).
19. K. Totsu, K. Fujishiro, S. Tanaka, and M. Esashi, Sens. Actuators A **130**, 387 (2006).
20. R. U. M. Haque, and K. D. Wise, J. Microelectromech. Syst. **22**, 1470 (2013).
21. D. Urbonas, A. Balčytis, K. Vaškevičius, M. Gabalis, and R. Petruškevičius, Opt. Lett., **41**, 3655 (2016).
22. A. N. Broers, A. C. F. Hoole, and J. M. Ryan, Microelectron. Eng. **32**, 131 (1996).
23. H. Jansen, M. de Boer, R. Wiegerink, N. Tas, E. Smulders, C. Neagu, and M. Elwenspoek, Microelectron. Eng. **35**, 45 (1997).
24. Z. Shao, Y. Chen, H. Chen, Y. Zhang, F. Zhang, J. Jian, Z. Fan, L. Liu, C. Yang, L. Zhou, and S. Yu, Opt. Express **24**, 1865 (2016).
25. Z. Shao, Y. Zhang, S. Li, L. Liu, C. Yang, L. Zhou, H. Chen, Y. Chen, and S. Yu, *Asia Communications and Photonics Conference* (Optical Society of America, 2016), paper AF4E. 4.
26. M. Stalder, and M. Schadt, Opt. Lett. **21**, 1948 (1996).
27. I. Moreno, J. A. Davis, I. Ruiz, and D. M. Cottrell, Opt. Express **18**, 7173 (2010).